33RD CONGRESS
OF THE INTERNATIONAL COUNCIL
OF THE AERONAUTICAL SCIENCES
STOCKHOLM, SWEDEN, 4-9 SEPTEMBER, 2022

ICAS 2022 SWEDEN

EXPERIMENTAL ANALYSIS OF HEAT TRANSFER CHARACTERISTICS OF DIELECTRIC BARRIER DISCHARGE PLASMA ACTUATOR

Asami Hatamoto[1], Kenta Emori[2], & Hiroyuki Nishida[3]

[1,2,3]Department of Mechanical Systems Engineering, Tokyo University of Agriculture and Technology

Abstract

The dielectric barrier discharge plasma actuator (DBDPA) is an active flow control device that induces the wall surface jet utilizing the electrohydrodynamic force coming from the atmospheric barrier discharge. In recent years, heat transfer enhancement, de-and anti-icing using DBDPA gets much attention. In the applications of DBDPA to the field of thermal engineering, it is important to understand the thermal characteristics of DBDPA itself. The purpose of this study is to clarify the heat transfer characteristics of DBDPA. For this purpose, the heat transfer coefficient and temperature of the wall-surface jet are estimated by fitting the analytical solution of the one-dimensional heat conduction inside the actuator. The time variation of temperature of the dielectric surface is measured using the IR camera. The measurement is performed by varying the applied voltage. Additionally, the time range and region for which the assumption of one-dimensional heat conduction is valid are identified by the numerical simulation of two-dimensional heat conduction. As a result, the heat transfer coefficient and airflow temperature are larger at higher voltages and take their maximum values near the electrode, and these values are expected to be qualitatively valid. In the future research, to discuss the quantitative nature of the estimates, flow field measurements, discharge imaging, and thermal energy calculations are conducted.

Keywords: Wall Surface Jet, Dielectric Barrier Discharge, Heat Transfer, Plasma Actuator

1. Introduction

Ice on wings of aircraft can cause flow separation, increasing drag and reducing lift. The dielectric barrier discharge plasma actuator (DBDPA) is attracting attention as a device to prevent wing icing and de-icing [1]–[4]. The DBDPA consists of two electrodes separated by dielectric, and one electrode is exposed to the air, and the other is encapsulated by the dielectric as shown in Fig. 1. The wall-surface discharge is generated by applying the AC high voltage of typically up several tens kV and several kHz. This discharge generates the electrohydrodynamic (EHD) force, which induces a wall jet. The DBDPA has many advantages [5] such as thin and light, no mechanical moving parts, and electrical rapid controllability. The DBDPA can manipulate the flow by the EHD force and has been studied for various engineering applications such as flow separation control of aerodynamic bodies [6]–[8], boundary layer transition control [9], [10], and noise reduction [11].

As shown in Fig. 2, most of the power consumed by the DBDPA is converted into heat[12], which rises the temperature of surrounding airflow and walls. In order to apply the DBDPA as a heater for anti-icing and de-icing, a fundamental investigation of the thermal characteristics of the device is necessary. Previous research has been conducted to measure surface temperature using infrared cameras [13]–[15]. To discuss the heat energy input to the airflow and the wall, the heat transfer coefficient and the airflow temperature rising need to be clarified. However, the airflow temperature measurement near the electrode is difficult because the thickness of the discharge region is very thin, micrometer order, and the high voltage is applied to the top electrode.

The objective of this study is to quantitatively calculate the temperature and heat transfer coefficient of the airflow induced by DBDPA. For this purpose, we measure the surface temperature of the DBDPA and fit the analytical solution of the heat conduction equation to it. In this paper, as an first step of the research, we investigate the DBDPA driving in quiescent air.

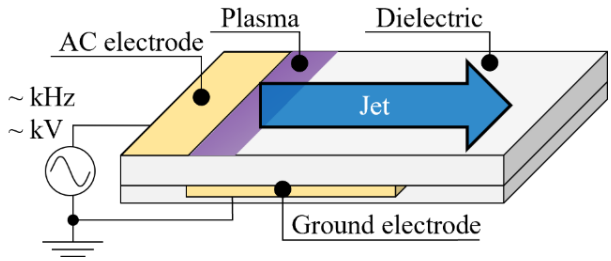

Figure 1 – Schematic of the DBDPA.

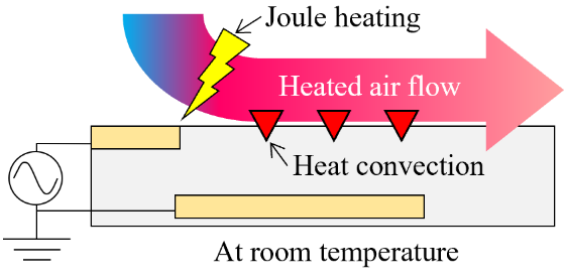

Figure 2 – Schematic of heat production and transfer process around the DBDPA.

2. Experimental and Analytical Methods

2.1 Setup for Surface Temperature Measurement

Top view of the surface temperature measurement is shown in Fig. 3. The temperature of the DBDPA is measured by the infrared camera (FLIR, T630). The spectral range of the camera is 7.5–14 μm, the frame rate is 30 Hz, the temperature resolution is 0.03 K, and size of thermal photograph is 640 x 480 pixel. The spatial resolution is about 0.25 mm per 1 pixel. The measurement time is 300 seconds (9001 frames) from plasma ignition. The bottom of the DBDPA is insulated with Styrofoam, which has a thermal conductivity of 0.036. For the analysis, the one-dimensional temperature distribution of the DBDPA is obtained by averaging in the spanwise direction.

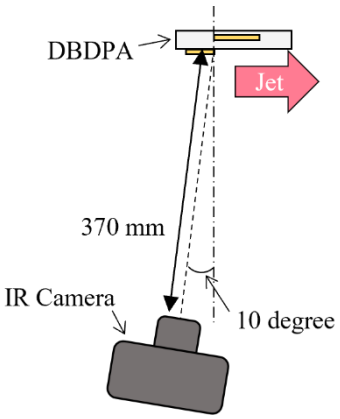

Figure 3 – Setup for measurement of surface temperature.

The configuration of the DBDPA is shown in Fig. 4. The material of the electrode is copper tapes, the thickness is 0.05 mm, the bottom electrode is covered with polyimide tape, and there is no gap between two electrodes. The surface of the top electrode is painted with the black splay to specify the emissivity. The dielectric is PMMA (polymethyl methacrylate), and the physical properties of the dielectric materials are shown in Table 1. The emissivity of the dielectrics are values obtained from the preliminary surveys, and others are the nominal value.

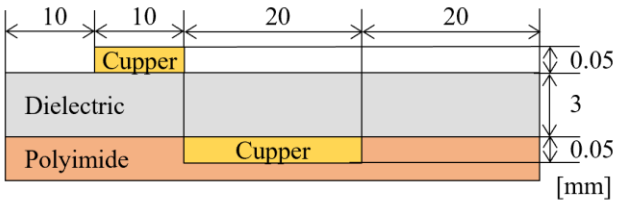

Figure 4 – Configuration of the DBDPA.

Table 1. Physical properties; emissivity e, thermal conductivity k, density ρ, specific heat capacity c, and permittivity ε.

Dielectric	e	k [W/m · K]	ρ [kg/m^3]	c [J/kg · K]	ε
PMMA	0.96	0.21	1.2 ×10^3	1.46×10^3	3.1

The voltage signal of the AC high voltage is supplied from the function generator (Tektronix, AFG2021), and the signal is amplified by the amplifier (Trek, 20/20A-HS). The applied high voltage is monitored with the oscilloscope (Teledyne LeCroy, HDO4034) via the high voltage prove (IWATSU, PHV4002-3-RO). The wave form of the AC voltage is sinusoidal, and the frequency of the voltage is 1 kHz. The experiment is conducted by varying the amplitude of the voltage to 18, 20, and 22 kV_{pp}.

2.2 Simulation Method for Heat Conduction

The temperature distribution inside the dielectric of the DBDPA is obtained by the numerical simulation. The governing equation is the two-dimensional heat conduction equation:

$$\frac{\partial \theta}{\partial Fo} = \frac{\partial^2 \theta}{\partial Y^2} + \frac{\partial^2 \theta}{\partial Z^2}, \tag{1}$$

where θ is dimensionless temperature, Fo is Fourier number, and Y and Z is dimensionless length. The computational domain is the inside of the dielectric with a thickness of 3 mm and a length of 60 mm, as shown in Fig. 5, and the physical properties of the dielectric are shown in Table 1. In the spanwise direction, the temperature distribution is assumed to be uniform. The boundary condition on the top surface is the surface temperature measured in the experiment. The experimental temperature is averaged in the spanwise direction and interpolated linearly. Note that the thickness of the top electrode is ignored. The boundary conditions for other surfaces are the thermal insulation, and the initial condition is room temperature. The time integration is calculated by the second order Runge–Kutta method, and the spatial differential is calculated by the second order central difference method. The time increment dt is 0.008 s, the spatial grid sizes dy and dz are 0.08 mm.

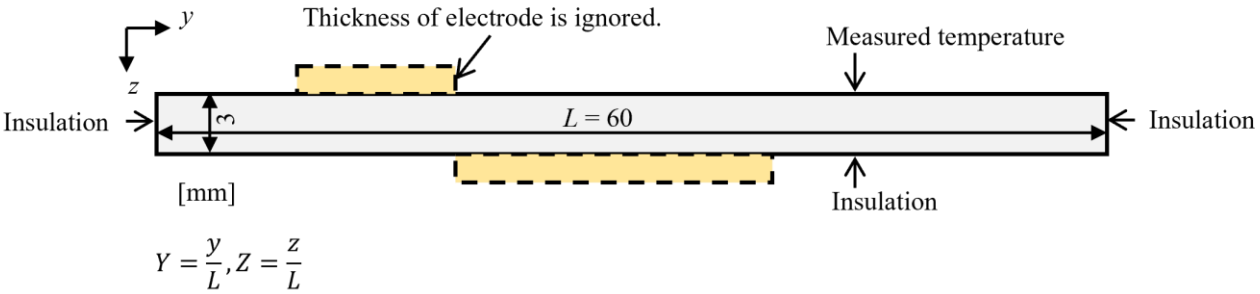

Figure 5 – Simulation domain.

2.3 Estimation Method for Heat Transfer Coefficient and Airflow Temperature

The heat transfer coefficient and the airflow temperature are estimated by regression using the time-profile of surface temperature [16], [17]. Assuming one-dimensional heat conduction in the thickness direction in the dielectric, the airflow temperature does not vary in time, the heat is transferred from the airflow to the dielectric at a constant heat transfer coefficient, and the dielectric is a semi-infinite solid in the thickness direction, the surface temperature of the dielectric is obtained as [18]

$$\frac{T - T_{\mathrm{i}}}{T_{\mathrm{f}} - T_{\mathrm{i}}} = 1 - \exp\left(\frac{h^2 \alpha t}{k^2}\right) \mathrm{efrc}\left(\frac{h\sqrt{\alpha t}}{k}\right), \tag{2}$$

where T is the surface temperature, T_{i} is the initial temperature (room temperature), T_{f} is the airflow temperature, h is the heat transfer coefficient, α is thermal diffusivity, and k is thermal conductivity. The heat transfer coefficient and temperature of the wall-surface jet are estimated by fitting Eq (2) to the surface temperature obtained by the experiment.

3. Result and Discussion

3.1 Surface Temperature Characteristics

Figure 6 shows the thermal photograph when the applied voltage is 22 kV_{pp} and the time of 300 s after the start of plasma ignition. The temperature at the left and right ends of the electrode is masked because there are exposed and highly reflective and cannot be measured. A non-uniformity in the span direction (x-direction) is observed in the temperature distribution. This is due to the micro-discharge, which is a typical discharge structure of dielectric barrier discharge. Therefore, the average temperature in the spanwise direction is used for the subsequent analysis. Figure 7 shows the *y* (distance from the electrode edge) profile surface temperature at 5, 50, and 300 s after the start of plasma ignition and when the applied voltage is 22 kV_{pp}. The temperature change is the difference from the room temperature, and it is averaged in the spanwise direction (the range is from *x* = -30 mm to 30 mm). The temperature is the highest at the edge of the electrode and decreases with distance from the edge of the electrode. This is because the heat is generated in the discharge region near the electrode edge.

Figures 8 shows the time variation of the surface temperature at *y* = 2 and 10 mm. Near the electrode, the temperature rises rapidly after discharge ignition, whereas at downstream the temperature rises more slowly. The higher the applied voltage is, the higher the surface temperature is because power consumption becomes higher. The temperature does not become steady even 300 seconds after the start of discharge.

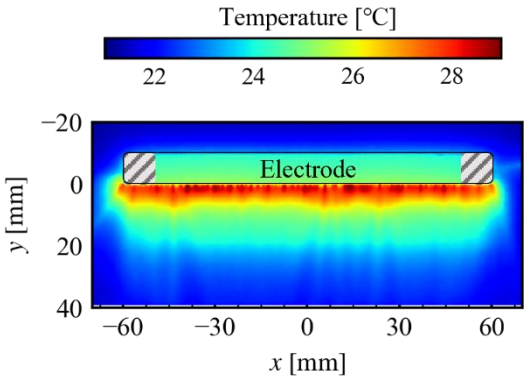

Figure 6 – Thermal photograph of DBDPA when the applied voltage is 22 kV_{pp} and *t* = 300.

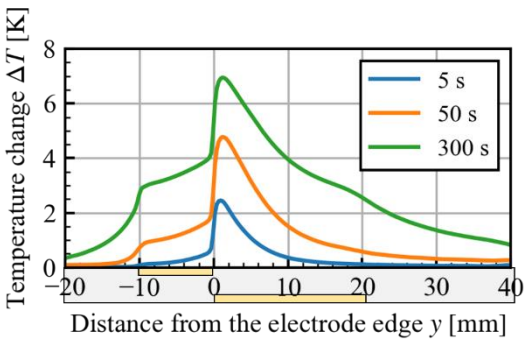

Figure 7 – Temperature distribution when the applied voltage is 22 kV_{pp}.

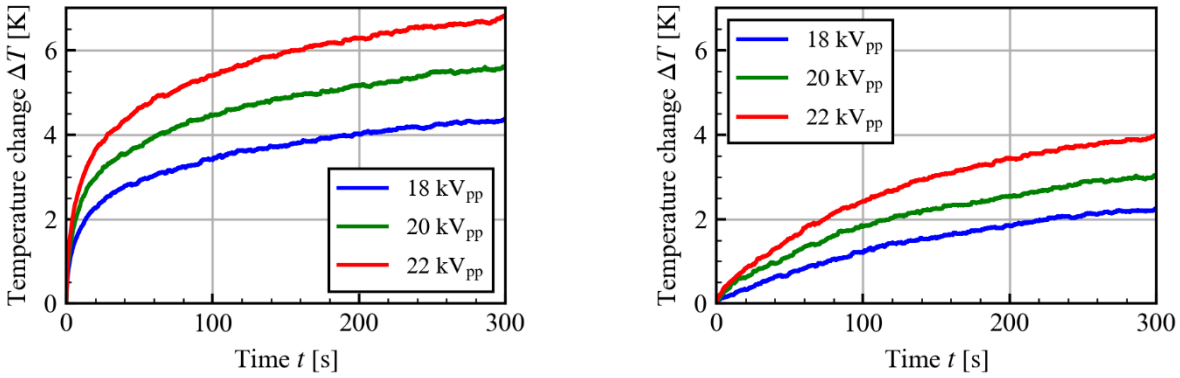

(a) y = 2 mm (b) y = 10 mm

Figure 8 – Time variation of surface temperature.

3.2 Heat Conduction Inside Dielectric

In this paper, the semi-infinite solid assumption and the one-dimensional heat conduction assumption are used in the derivation of Eq. (2). The time range and region where this assumption is valid can be identified based on the simulation results the temperature and heat flux distributions. Figure 9 shows the temperature distribution inside the dielectric at t = 10 s and 300 s obtained by the numerical simulation when the applied voltage is 22 kV_{pp}. The plotted value is the amount of change from the room temperature. The heat diffusion inside the dielectric is successfully reproduced.

Figure 10 shows the heat flux field when the applied voltage is 22 kV_{pp} and t = 1 s. The colors in the contour plot show temperatures, and the vectors show heat fluxes. The heat flux is calculated from the temperature gradient. We assume that one-dimensional heat conduction is valid in the region where the y component of the heat flux is less than 10 % of the z component. In Fig. 10, one-dimensional heat conduction is valid in the region y > 0.5 mm. Additionally, heat does not reach the underside of the dielectric, and a semi-infinite solid assumption is also valid. Therefore, the temperature data at t = 0–1 s and y > 0.5 mm are used for fitting using Eq. (2).

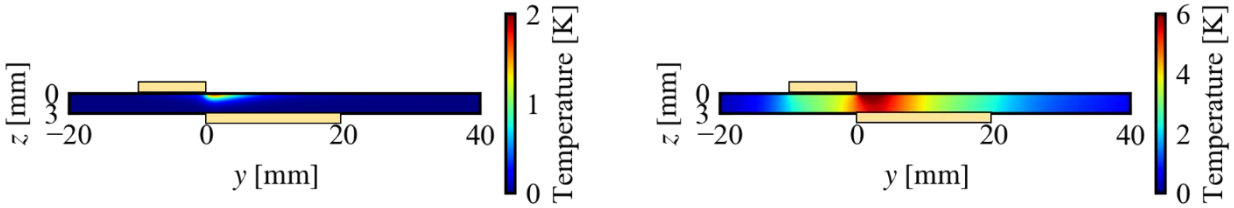

(a) t = 10 s (b) t = 300 s

Figure 9 – Temperature distribution inside the dielectric when the applied voltage is 22 kV_{pp}.

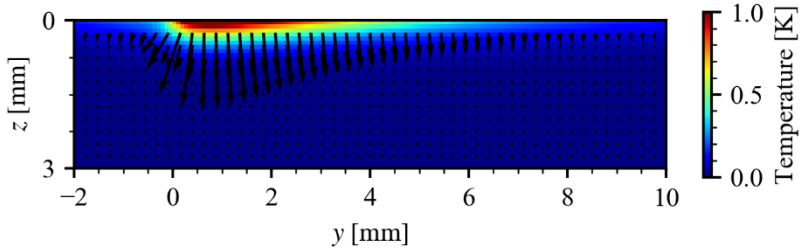

Figure 10 – Heat flux field when the applied voltage is 22 kV_{pp} and t = 1 s.

3.3 Estimation Result

Figure 11 shows the fitting result of the analytical solution (Eq. (2)) to the time-variation of temperature at y = 2 mm and 10 mm. The solid line is experimental value, and dotted line is the fitted line. The analytical solutions are almost fitted to the experimental results, however, the discrepancies are large at from t = 0.0 s to 0.3 s. This discrepancy is considered to be due to the formation stage of the steady wall-surface jet just after the start of the DBDPA driving.

Figures 12 and 13 show the estimated heat transfer coefficient and the airflow temperature by fitting. Note that the area up to 0.5 mm from the edge of the electrode is masked because it is the area where two-dimensional heat conduction occurs and cannot be estimated correctly. As shown in Fig. 12, the estimated heat transfer coefficient decreases from upstream to downstream. This characteristic is correlated with the velocity distribution of the induced flow by DBDPA. Additionally, the value becomes larger as the applied voltage increases. The induced flow velocity of DBDPA also increases with applied voltage, so the estimation is expected to be qualitatively correct. As shown in Fig. 13, the estimated airflow temperature becomes maximum at the location about 1 mm downstream from the electrode. This is because the heating area spreads downstream due to the wall-surface discharge, and the air temperature continue to rise during convection from the electrode edge to downstream. Moreover, the higher the applied voltage is, the higher the airflow temperature becomes. This is because the discharge becomes stronger and more power is consumed.

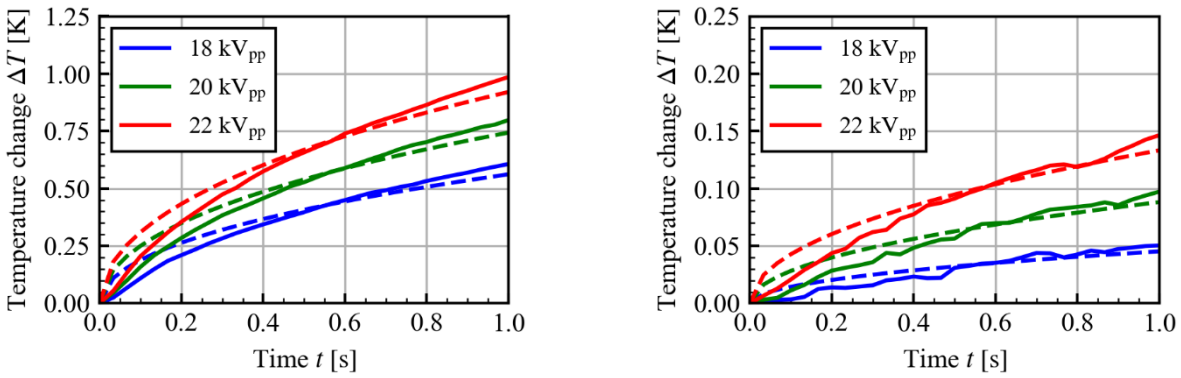

(a) y = 2 mm (b) y = 10 mm

Figure 11 – Time variation of surface temperatures at y = 2 mm obtained by measurement (solid line) and fitting (dashed line).

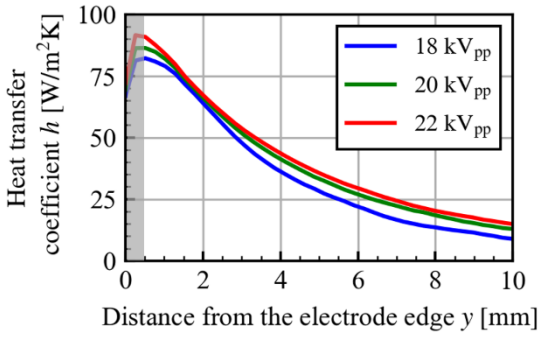

Figure 12 – Estimated heat transfer coefficient.

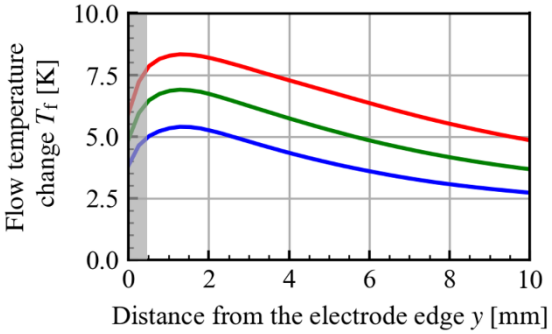

Figure 13 – Estimated airflow temperature.

4. Conclusion

In this paper, the heat transfer coefficient and airflow temperature distribution of the DBD plasma actuator were estimated from the surface temperature by assuming one-dimensional heat conduction in the dielectric. As a result, the calculated values were found to be qualitatively correct. In the future research, to discuss the quantitative nature of the estimates, flow field measurements, discharge imaging, and thermal energy calculations are required.

5. Contact Author Email Address

Corresponding author's e-mail: hnishida@cc.tuat.ac.jp

6. Copyright Statement

Acknowledgments

This work was supported by JSPS KAKENHI Grant Number 19H02062, 20KK0104.

References

[1] J. Chen *et al.*, “Experimental Study on Anti-Icing Performance of NS-DBD Plasma Actuator,” *Appl. Sci.*, vol. 8, no. 10, p. 1889, Oct. 2018.

[2] Y. Liu, C. Kolbakir, H. Hu, and H. Hu, “A comparison study on the thermal effects in DBD plasma actuation and electrical heating for aircraft icing mitigation,” *Int. J. Heat Mass Transf.*, vol. 124, pp. 319–330, Sep. 2018.

[3] B. Wei *et al.*, “SDBD based plasma anti-icing: A stream-wise plasma heat knife configuration and criteria energy analysis,” *Int. J. Heat Mass Transf.*, vol. 138, pp. 163–172, Aug. 2019.

[4] C. Kolbakir, H. Hu, Y. Liu, and H. Hu, “An experimental study on different plasma actuator layouts for aircraft icing mitigation,” *Aerosp. Sci. Technol.*, vol. 107, p. 106325, Dec. 2020.

[5] T. C. Corke, M. L. Post, and D. M. Orlov, “SDBD plasma enhanced aerodynamics: concepts, optimization and applications,” *Prog. Aerosp. Sci.*, vol. 43, no. 7, pp. 193–217, Oct. 2007.

[6] K. Fujii, “Three Flow Features behind the Flow Control Authority of DBD Plasma Actuator: Result of High-Fidelity Simulations and the Related Experiments,” *Appl. Sci.*, vol. 8, no. 4, p. 546, Apr. 2018.

[7] S. Shimomura, S. Sekimoto, A. Oyama, K. Fujii, and H. Nishida, “Closed-Loop Flow Separation Control Using the Deep Q Network over Airfoil,” *AIAA Journal*, vol. 58, no. 10, pp. 4260–4270, Oct. 2020.

[8] X. Zhang, K.-S. Choi, Y. Huang, and H.-X. Li, “Flow control over a circular cylinder using

virtual moving surface boundary layer control," *Exp. Fluids*, vol. 60, no. 6, p. 104, May 2019.

[9] D. Opaits, D. Roupassov, S. Starikovskaia, A. Starikovskii, I. Zavialov, and S. Saddoughi, "Plasma Control of Boundary Layer Using Low-Temperature Non-equilibrium Plasma of Gas Discharge," in *43rd AIAA Aerospace Sciences Meeting and Exhibit*, American Institute of Aeronautics and Astronautics, 2005.

[10] G. I. Font, "Boundary Layer Control with Atmospheric Plasma Discharges," *AIAA Journal*, vol. 44, no. 7, pp. 1572–1578, Jul. 2006.

[11] F. O. Thomas, A. Kozlov, and T. C. Corke, "Plasma Actuators for Cylinder Flow Control and Noise Reduction," *AIAA Journal*, vol. 46, no. 8, pp. 1921–1931, Aug. 2008.

[12] F. Rodrigues, J. Pascoa, and M. Trancossi, "Heat generation mechanisms of DBD plasma actuators," *Exp. Therm. Fluid Sci.*, vol. 90, pp. 55–65, Jan. 2018.

[13] R. Tirumala, N. Benard, E. Moreau, M. Fenot, G. Lalizel, and E. Dorignac, "Temperature characterization of dielectric barrier discharge actuators: influence of electrical and geometric parameters," *J. Phys. D Appl. Phys.*, vol. 47, no. 25, p. 255203, May 2014.

[14] F. F. Rodrigues, J. C. Pascoa, and M. Trancossi, "Experimental Analysis of Dielectric Barrier Discharge Plasma Actuators Thermal Characteristics Under External Flow Influence," *J. Heat Transfer*, vol. 140, no. 10, p. 102801, May 2018.

[15] L. Shen, Z. Chen, and C. Y. Wen, "Thermal Effect on the Performance of an Alternating-Current Dielectric-Barrier-Discharge Plasma Actuator," *AIAA Journal*, vol. 58, no. 8, pp. 3368–3377, Aug. 2020.

[16] T. N. Jukes, K.-S. Choi, T. Segawa, and H. Yoshida, "Jet flow induced by a surface plasma actuator," *Proc Inst Mech Eng Part I J Syst Control Eng*, vol. 222, no. I5, pp. 347–356, May 2008.

[17] R. Joussot, V. Boucinha, R. Weber-Rozenbaum, and D. Hong, "Thermal Characterization of a DBD Plasma Actuator: Dielectric Temperature Measurements Using Infrared," in *40th Fluid Dynamics Conference and Exhibit*, 2010.

[18] F. Kreith, R. M. Manglik, and M. S. Bohn, *Principles of Heat Transfer*. Cengage Learning, 2011.